Arjas, Kristian; Taskinen, Jani Matti; Heilmann, Rebecca; Salerno, Grazia; Törmä, Päivi

High topological charge lasing in quasicrystals

Published in:
Nature Communications

DOI:
10.1038/s41467-024-53952-5

Published: 01/12/2024

Document Version
Publisher's PDF, also known as Version of record

Please cite the original version:
Arjas, K., Taskinen, J. M., Heilmann, R., Salerno, G., & Törmä, P. (2024). High topological charge lasing in quasicrystals. *Nature Communications*, *15*(1), 1-10. Article 9544. https://doi.org/10.1038/s41467-024-53952-5

nature communications

Article https://doi.org/10.1038/s41467-024-53952-5

High topological charge lasing in quasicrystals

Received: 6 May 2024

Accepted: 28 October 2024

Published online: 05 November 2024

Check for updates

Kristian Arjas[1,2], Jani Matti Taskinen[1,2], Rebecca Heilmann[1], Grazia Salerno[1] & Päivi Törmä[1]

Photonic modes exhibiting a polarization winding akin to a vortex possess an integer topological charge. Lasing with topological charge 1 or 2 can be realized in periodic lattices of up to six-fold rotational symmetry—higher order charges require symmetries not compatible with any two-dimensional Bravais lattice. Here, we experimentally demonstrate lasing with topological charges as high as −5, +7, −17 and +19 in quasicrystals. We discover rich ordered structures of increasing topological charges in the reciprocal space. Our quasicrystal design utilizes group theory in determining electromagnetic field nodes, where lossy plasmonic nanoparticles are positioned to maximize gain. Our results open a new path for fundamental studies of higher-order topological defects, coherent light beams of high topological charge, and realizations of omni-directional, flat-band-like lasing.

Topological defects are ubiquitous in nature, both in quantum and classical fields[1]. They may manifest as winding of the phase of a scalar field or of a vector quantity (spin, polarization) when encircling a point either in real or reciprocal space. Such winding can exhibit only integer values and is thereby topologically protected against small perturbations[2,3]. While some topological defects form spontaneously, others can originate from the structure and/or symmetries of the system. Topological defects may also form periodic or otherwise ordered textures[4,5].

In optical systems, vortices of polarization with a topological charge of $q = \pm1$, -2 or -3 have been created utilizing bound states in continuum (BICs)[6–15]. BICs show a winding of the light polarization around a specific momentum (**k**) point, causing the polarization to be undefined in the **k**-point itself and forcing the electromagnetic field to zero akin to a vortex core. Consequently, there is no far-field light radiating out of the system at that momentum (direction): BICs are dark states. Various leakage mechanisms[16–19] can be designed to allow the emission of light from a BIC; such modes are called quasi-BICs. By combining the structure with a gain medium, one may realize lasing in BICs[18–35] to create sources of coherent light beams with polarization windings that are topologically protected. Such vector vortex beams, with winding in a vector quantity (polarization), are distinct from optical angular momentum beams which have a vortex in a scalar quantity (phase)[11,36–39]. Combinations of BICs offer new possibilities for realizing also beams with high orbital angular momentum[11].

Here we propose a method of designing plasmonic structures with noncrystallographic symmetries and demonstrate control over the mode energies via the ohmic losses inherent to metallic nanoparticles. This allows us to realize lasing with very high values of the topological charge q that characterizes polarization winding in the lasing beam. We fabricate the samples and experimentally measure lasing 8-, 10- and 12-fold rotationally symmetric structures with topological charges $q = -3$, -4, and -5 with the third sample also exhibiting transitions to as high values of q as +19 at higher angles.

Results

Plasmonic quasicrystal design

To induce lasing with a polarization vortex of topological charge greater than two, at the first Γ-point of the reciprocal space, rotational symmetries higher than six-fold are required. However, such symmetries are incompatible with the crystallographic restriction theorem of periodic lattices in two dimensions. Realizations of lasing in quasicrystals so far have used the Penrose tiling or similar designs with rotational symmetry[40–42], but did not explore the potential of the high topological charges[43]. Quasicrystals host several modes with different topological charges, up to the highest one allowed by their symmetry.

[1]Department of Applied Physics, Aalto University School of Science, Espoo, Finland. [2]These authors contributed equally: Kristian Arjas, Jani Matti Taskinen. e-mail: paivi.torma@aalto.fi

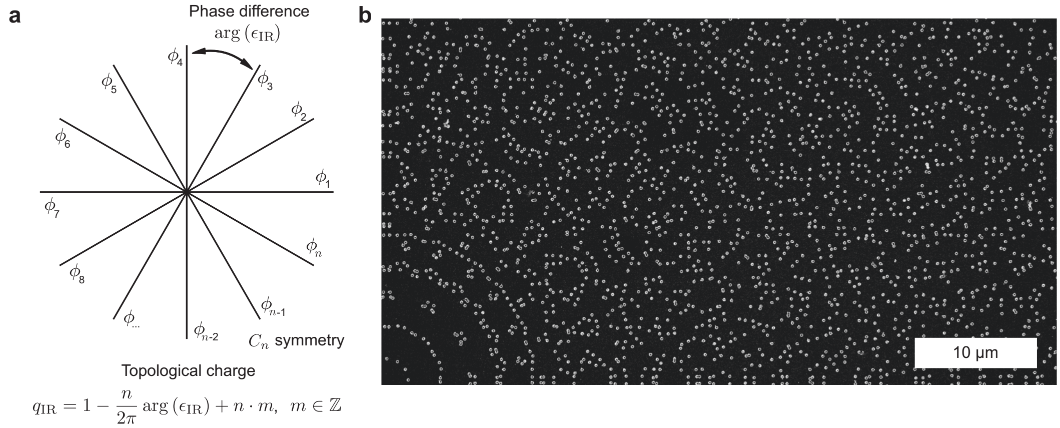

Fig. 1 | Quasicrystal design. a A system with n-fold rotational symmetry (C_n) can be constructed by combining a set of n plane-waves with phase factors $\exp(i\phi_i)$. The phases must satisfy $\phi_{i-1} = \arg(\epsilon_{\mathrm{IR}}) + \phi_i$ where ϵ_{IR} is the character of an IR of the symmetry group. By imposing the phase difference $\arg(\epsilon_{\mathrm{IR}})$ between the plane-waves and positioning lossy nanoparticles in the nodes of the interference pattern, lasing with the topological charge q_{IR} corresponding to the chosen IR can be enforced. **b** A scanning electron microscope image of a C_{12} symmetric quasicrystal sample, showing approximately 3 % of the total crystal area. Particle positions are available in Supplementary Data 1.

This poses a challenge: how can a specific charge be selected for lasing when there are different charge modes closely spaced in energy?

Plasmonic nanoparticles are associated with strong ohmic losses – a feature that we utilize in our approach. Combined with organic dye molecules under optical pumping, plasmonic nanoparticle arrays[44,45] have shown lasing with both conventional beam polarizations and topological charges[19,29–31,46–48]. We propose a quasicrystal design method that combines group theory with the lossy nature of these structures to experimentally realize lasing with charges higher than the previously observed ±1 and −2. We achieve polarization windings corresponding to −3, −4 and −5 in different samples specifically designed to support lasing in these modes. Surprisingly, the phenomena presented by the quasicrystals go remarkably beyond this. We discover a rich structure of polarization vortices in the reciprocal space, including topological charges as extreme as −17 and +19.

We start by defining a two-dimensional quasicrystal with a given symmetry such that it provides high topological charges. The charge q counts how many times the polarization vector rotates along a path $\mathcal{C}$ centered on the vortex core in momentum space: $q = \frac{1}{2\pi}\oint_{\mathcal{C}} d\mathbf{k} \cdot \nabla_{\mathbf{k}}\Phi(\mathbf{k})$[6]. The phase of the polarization vector, describing the field orientation is calculated from the Stokes parameters $\Phi(\mathbf{k}) = \frac{1}{2}\arctan(S_2(\mathbf{k})/S_1(\mathbf{k}))$ and is related to the irreducible representations (IRs) of the underlying rotational symmetry of the optical system[31]. In group theory, the character ϵ_{IR} tabulates the IRs under the n-fold rotational symmetry C_n, with the phase change under rotation described by the argument of the character. In scalar fields, these describe the different angular momentum states that can exist in the system[39]. The topological charge q on the other hand, is a property of vector fields and connects to the orbital angular momenta (l) of its components, as is explicitly shown in Supplementary Note 1. The allowed topological charges q for a mode belonging to a given IR are expressed as[31]

$$q_{\mathrm{IR}} = 1 - \frac{n}{2\pi}\arg(\epsilon_{\mathrm{IR}}) + n \cdot m \text{ and } m \in \mathbb{Z}. \tag{1}$$

For C_n where n is even, the IRs labeled as B have the strongest response to rotation with $\arg(\epsilon_{\mathrm{IR}}) = \pi$[49], corresponding to greatest field winding resulting in the topological charge $q_B = 1 - n/2$ (for $m = 0$). From this, it is obvious that charges $|q| \geq 3$ require quasicrystals with at least eight-fold symmetry $n \geq 8$.

Quasicrystals are defined as ordered non-periodic structures. Any rotational symmetry other than C2, C3, C4, or C6 implies non-periodicity by the crystallographic restriction theorem. The order, on the other hand, is evident as n-fold symmetric Bragg diffraction points $\mathbf{G_n}$[40]. Our quasicrystal design method is based on electric field interference patterns formed from standing waves with wavevectors $\mathbf{G}_i$ corresponding to the first-order Bragg peaks. When the phase relation between these standing waves is chosen to satisfy the B IR character under C_n, the mode will host a polarization vortex with the highest available charge. We enforce lasing with the chosen topological charge by placing cylindrical gold nanoparticles in the low-intensity regions of the resulting interference pattern. As a result, the ohmic losses of the desired mode are minimized, while the modes belonging to other IRs are greatly dampened. See Fig. 1a for a simple illustration of the concept. Notably, we found the design given by the interference pattern minima to be significantly different from quasicrystals generated from well-known aperiodic tessellations, such as the Penrose or Ammann-Beenker tilings. These tilings define a full set of points leaving no room for selection of particular topological charges. In addition to the main principle depicted in Fig. 1a, our design method involves two additional steps to restore quasiperiodicity by a moiré pattern and to equalize the nanoparticle density; see materials and methods, and Supplementary Note S2 for further information. Our design method produces structures that have the properties of a quasicrystal, namely order (see the structure factor in Supplementary Fig. S1) and non-periodicity (by the crystallographic restriction theorem). The Bragg diffraction points of the quasicrystal provide possible feedback for lasing akin to the distributed feedback lasing mechanism.

The nanoparticles are fabricated on borosilicate glass substrates and overlaid with a solution of IR-140 dye molecules. The diameter of the circular quasicrystal structures is set to 290 μm and the nanoparticles have radii of 80–130 nm. The structure layout is designed to support modes at the target free-space wavelength of 580 nm; with the refractive index of the dye ($n_r \approx 1.52$), the mode wavelength becomes 882 nm where the absorption and emission properties of the dye are suitable for lasing. Figure 1b presents an example of a fabricated quasicrystal sample. The emission patterns presented in this article are measured from structures with 8-, 10-, and 12-fold rotational symmetry, holding topological charges −3, −4, and −5, respectively. We excite the molecules using 100 fs laser pulses at 800 nm center wavelength and capture the emission properties of the sample. See materials and methods for details on the fabrication process and the experiments.

High topological charge lasing

We first discuss the results featuring the highest-obtained topological charges. At sufficient pump fluence, an angle-resolved image of the

https://doi.org/10.1038/s41467-024-53952-5

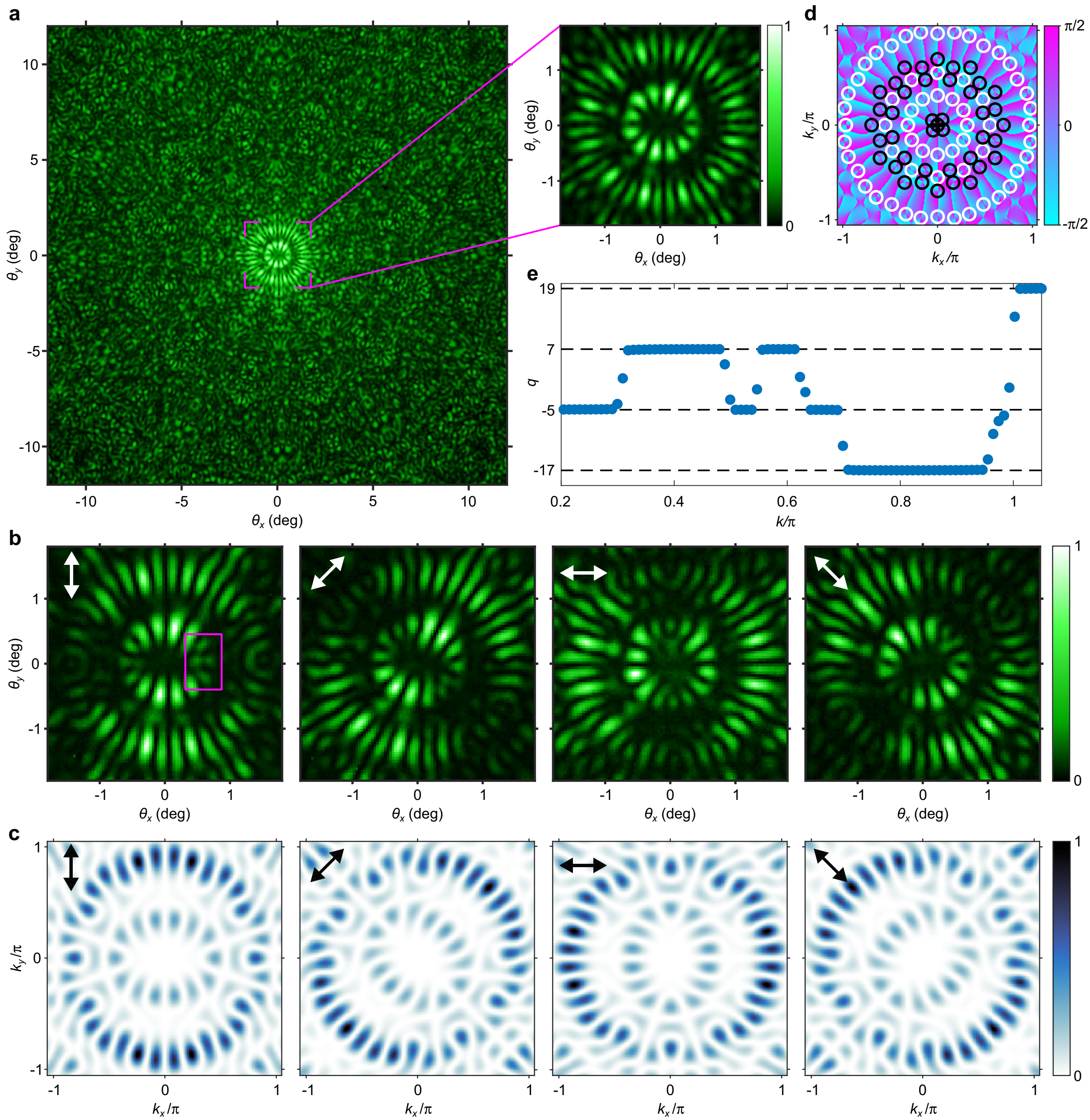

Fig. 2 | High topological charge lasing in plasmonic quasicrystal modes. a Angle-resolved image of lasing action exhibiting a topological charge of −5 in the center. The angle $\theta_{x,y}$ corresponds to the in-plane momentum via $k_{x,y} = 2\pi/\lambda_0 \sin(\theta_{x,y})$ where λ_0 is the wavelength in free space. The colorscale corresponds to normalized intensity. The data in the zoomed-out image are scaled using the natural logarithm to highlight the detailed emission patterns at wide angles; see Supplementary Fig. S5 for the linear scale version. **b** Polarization-resolved images of the lasing action shown in panel **a**. The white arrows denote the orientation of the linear polarization filter. The magenta rectangle highlights a location where the transition between two different topological charges causes one of the polarized emission lobes to split. This transition is qualitatively displayed in Supplementary Fig. S6. **c** Normalized amplitude of the theoretical mode, with the polarization direction denoted by black arrows. **d** Phase of the theoretical polarization in momentum space, as obtained from a coupled dipoles model. Black and white circles indicate the locations of −1 and +1 polarization vortices, respectively, forming a rich ordered structure. A single demonstrative transition is presented in Supplementary Fig. S7. **e** Total topological charge calculated from the phase in panel **d** on a circular path $\mathcal{C}$ of radius k centered at the Γ-point. Dashed lines correspond to the allowed charges in Eq. (1).

quasicrystal emission reveals two highly directional rings of laser light highlighted in Fig. 2a. These are accompanied by a multitude of less bright, yet still monochromatic ordered textures of light beams situated at increasing emission angles. This rich pattern stems directly from the quasicrystal diffraction peaks in reciprocal space, which are more densely distributed than a regular lattice due to the lack of translational symmetry. See Supplementary Fig. S2 for a real space image of the quasicrystal under optical pumping.

The topological charges incorporated in the experimentally measured emission patterns can be obtained by following the winding of the polarization state around the ring perimeter[6,19–21,23–35]; see Supplementary Fig. S3 for a brief demonstration with simple examples. To this end, we capture linearly polarized images of the lasing patterns, see Fig. 2b, and follow the rotation of the intensity maxima which reveal the polarization states. Interestingly, for the smaller circle ($|\theta| < 1°$), the lobes positioned perpendicular to the polarization direction appear to split between the inner and outer edge of the ring, an example of which is highlighted with a magenta rectangle. Such features suggest a transition between two different topological charges. Indeed, following the polarization states on the inner and outer edge display winding in opposite directions, and a closed loop around the ring results in winding numbers −5 and + 7, respectively. Additional polarization images are provided in Supplementary Fig. S4. A similar analysis on the larger emission ring ($|\theta| > 1°$) yields extremely high polarization windings of −17 and + 19, with the negative charge again found on the inner edge.

Our experimental findings are explained and corroborated by theoretical considerations. The theoretical modes of a smaller, 60 µm diameter portion of the structure are obtained through numerical simulations using the coupled-dipole approximation. The nanoparticles behave as dipoles, and their radiation properties are highly directional and polarization-dependent, effectively coupling momentum and polarization[50]. We determine the orientation of the electric dipole moment of each nanoparticle and calculate the electric field diffraction pattern and polarization in the reciprocal space (see materials and methods). First, in Fig. 2c the polarization-filtered amplitudes of the theoretical mode show similar features to the experimental images. Crucially, we obtain theoretical insight into the observed structure of consecutive topological charge circles of opposite sign (−5, + 7 and −17, + 19) from the polarization phase of the theoretical mode, shown in Fig. 2d, derived from the Stokes parameters. Namely, we identify an ordered structure of −1 and + 1 vortices of the polarization phase, denoted with black and white circles respectively. These vortex cores have a dark emission in momentum space, explaining the lobed structure of the rings observed in Fig. 2a. The total topological charge enclosed in a circular path of radius k as a function of the wavevector $k = \sqrt{k_x^2 + k_y^2}$ is calculated in Fig. 2e. Close to the Γ-point, the topological charge of the mode is −5, as expected from the structure design, but additional charges are present as k is progressively increased. We predict a total charge of $q = +7$, $q = -17$, and even $q = +19$ – exactly as observed in the experiment. These exceptionally high topological charges are allowed by Eq. (1) with $m = \pm 1, 2$.

As a demonstration of the robustness of our pattern design method, we also present lasing action in samples designed for topological charges −3 and −4 with C_8 and C_{10} symmetries, respectively. Angle-resolved images of the lasing emission in these samples are presented in Fig. 3a, b, which exhibit the desired topological windings. Additional measurements with patterns designed for lower topological charges are shown in Supplementary Fig. S8. In Fig. 3c–e, we provide the output intensities, spectra, and linewidths of the observed emission for all three quasicrystal structures presented here. Figure 3c shows the maximum intensity measured near the energy of the first Γ-point as a function of the pump fluence; the samples exhibit a rapid nonlinear increase in output intensity, indicating a clear lasing threshold. At high pump fluences, the spectra in Fig. 3d display sharp emission lines close to the designed wavelength of operation. The linewidths (full width at half maximum) of these lasing peaks above the threshold are shown in Fig. 3e. Although the observed lasing characteristics, i.e., wavelengths, thresholds, and linewidths, are similar to those found in an equivalent periodic system[51], we emphasize that the origin of the topological features is a truly higher-order mode and not simply a periodic lasing mode modulated by the quasicrystal structure, see Methods for details. No lasing is observed when pumping the samples with a small pump spot, or when the diameter of the crystals is smaller than 90 µm, due to the lack of feedback mechanism, see Supplementary Fig. S9. The detailed and complex real space and k-space images are already an indication of spatial coherence, but we have also directly demonstrated coherence across the entire structures using a Michelson interferometer in Fig. 3f–h, see also Supplementary Fig. S13.

Although the rings of laser light exhibiting the topological charges near the Γ-point constitute the strongest features of the lasing signal, a remarkably significant portion of the total output intensity is spread to wide emission angles, as highlighted in Fig. 2a. The angle-resolved spectrum for the sample exhibiting lasing with topological charge −5 in Fig. 4a shows the narrow-in-energy lasing peak extending across the entire measured k-space. Similar features are also found for the other quasicrystal patterns, see Supplementary Fig. S11. A comparison with the measured sample dispersion (Fig. 4b) and calculated quasi-band structure of the pattern (Fig. 4c) shows that the position of the topological charge rings in energy coincides with the Γ-point of the quasicrystal, yet the flat emission band cannot be directly explained by the strongest features found in the measured and calculated band structures. However, the structure factor of a quasicrystal is often self-similar, and in the limit of an infinite system the peaks of the structure factor, i.e., allowed momenta, fill the whole reciprocal space[40,41], although with decreasing weights; see Supplementary Fig. S14 for an illustration of this. Our experiment succeeded in involving a large number of these momenta in lasing, resulting in monochromatic emission to all observed angles, i.e., flat-band-like lasing. Such a feature is very distinct from the BIC lasing in periodic structures, where lasing in the intrinsically dark BIC mode becomes visible in far-field due to designed or inherent leakage[16–19]: the wavevector of the lasing beam is given by this outcoupling mechanism. In our case, the quasicrystal intrinsically facilitates the outcoupling with a broad range of wavevectors, owing to the large number of Bragg peaks present in the structure factor.

Discussion

In summary, we have experimentally observed lasing with high topological charges of polarization winding, up to −17 and + 19. This was made possible by a three-step quasicrystal design method which does not rely on Penrose tiling or other known aperiodic tessellations. The method utilizes lossy nanoparticles which act as dampeners for the light fields, and group theory for selecting their positions. The particles are placed at the minima of the interference pattern given by fields that correspond to a chosen IR of the symmetry group, which determines the desired topological charge. In order to successfully realize lasing, we further needed to restore the quasiperiodicity by a moiré pattern and to equalize the nanoparticle density. The quasicrystal lasing provided rich textures of multiple topological charges, matching theoretical coupled-dipole calculations. The momentum-resolved spectrum revealed lasing in an energetically narrow band that was nearly uniform over all the measured momentum values, i.e., emission angles. Such flat-band-like lasing is not expected from the main features of the structure factor, meaning that the lasing action is able to exploit the continuum of weak Bragg peaks of a quasicrystal.

To expand the scientific scope and applications of the phenomena observed here, the design method can be readily applied beyond plasmonic systems. One only needs to combine a gain medium with a lossy structure fabricated following our design principles. Therefore, extension to lossy photonic crystal materials, electrically pumped semiconductor gain media, and other technologically mature systems is possible. Since the different charges in the quasicrystal lasing occur at different angles of emission, one or a few of them can be easily selected and others removed by spatially blocking the beam angles that correspond to unwanted charges. Furthermore, since the appearance of multiple higher-order topological defects depends on the structure (e.g., they are absent in C_8), it should be possible to optimize each quasicrystal to support only a single charge. In this way, one can create coherent, bright beams of almost arbitrarily high topological charge. Both the polarization vortex beams studied here and phase vortex beams of optical angular momentum the OAM beams have applications such as optical trapping, optical communications, and sensing[52–54]. Compared to methods of creating polarization vortex beams in real space by spatial light modulators[53], our approach has several advantages: the small structure size, lack of

https://doi.org/10.1038/s41467-024-53952-5

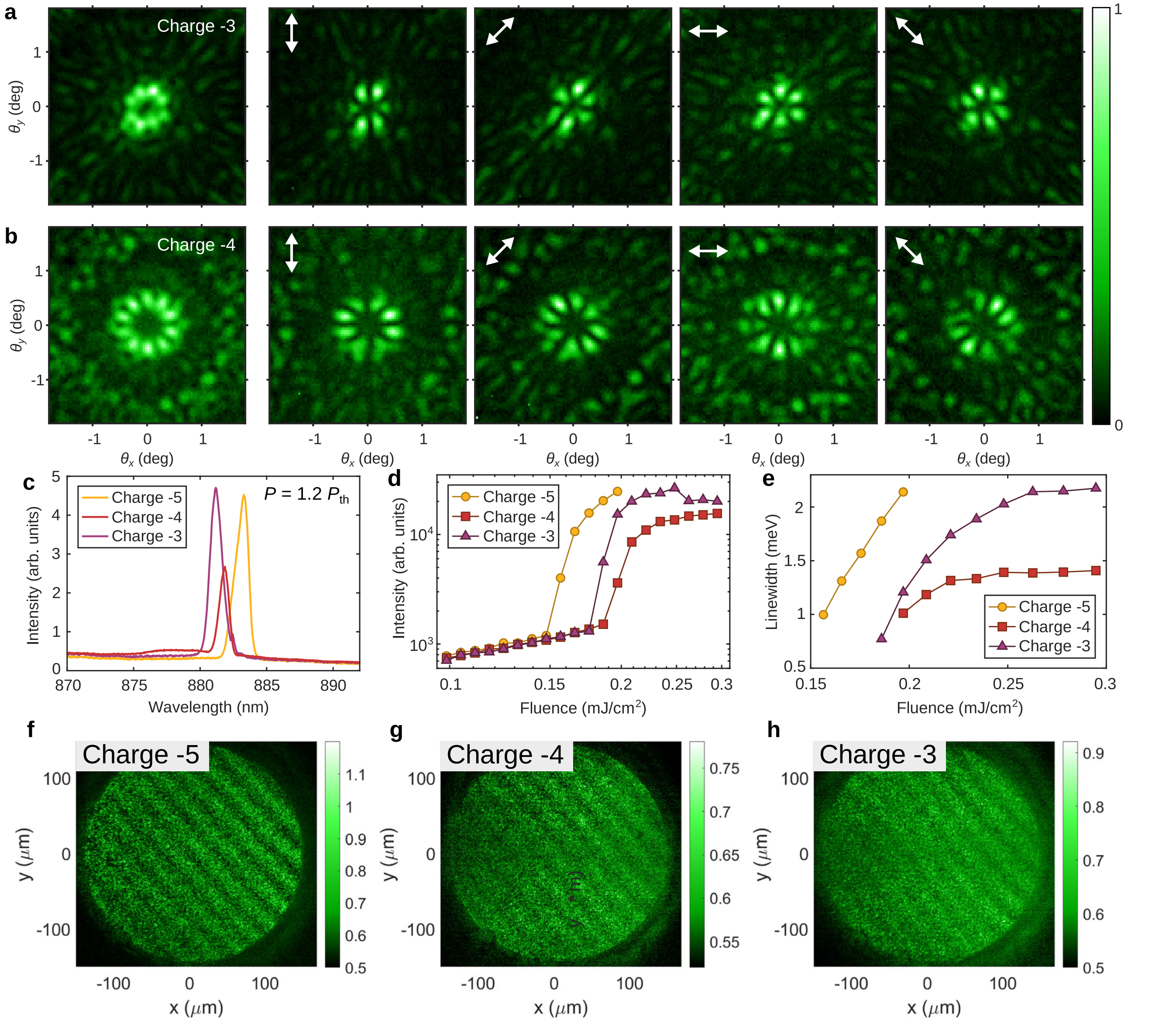

Fig. 3 | Lasing properties of plasmonic quasicrystal modes exhibiting topological charges −3, −4 and −5. a, b Angle-resolved lasing patterns showing topological charges −3 (**a**) and −4 (**b**). The white arrows denote the orientation of the linear polarization filter. The leftmost panel shows the unpolarized image. The color scale corresponds to normalized intensity. Theoretical modes are presented in Supplementary Fig. S10. **c** Peak output intensity as a function of pump fluence for samples designed for topological charges −3, −4, and −5. The spectra (**d**) and linewidths (**e**) of the lasing modes shown in panel **c**. The spectra are measured above the lasing threshold at $P = 1.2P_{th}$ where P_{th} corresponds to threshold pump fluence. Note that panel **e** presents linewidth values only above P_{th}; they cannot be resolved below the threshold due to low output intensity from the plasmonic modes, see Supplementary Fig. S11, **a** to **c**. The lasing linewidths at $1.2P_{th}$ correspond to quality factors of 809, 1050, and 751 for the charges −3, −4, and −5, respectively. The background-normalized interference patterns of the lasing quasicrystal structures with charges −5 (**f**), −4 (**g**), and −3 (**h**) acquired with a Michelson interferometer, details of which can be found in Supplementary Fig. S12. Interference patterns for different pump fluences can be found in Supplementary Fig. S13. The particle positions for the C_{10} and C_8 samples are available as Supplementary Data 2 and 3, respectively.

additional optics, and increased robustness of the emission to real-space perturbations due to having the polarization vortex in momentum space. The orthogonality of the modes with different topological charges gives a robust additional degree of freedom of light that could be utilized, for example, in multiplexing optical signals[55], and for quantum technologies[56]. On the other hand, the flat-band-like nature of the lasing can be utilized whenever emission to a wide angle range is desired together with better control of monochromaticity, coherence, and polarization than what random lasers[57,58] can offer.

Our results inspire further fundamental studies, for example, what are the highest topological charges that can be realized? Do the decay laws of spatial and temporal coherence in high-topological-charge lasing deviate from the usual ones? High optical angular momentum beams have become increasingly important because they can allow dipole-forbidden transitions and topological pumping, both in atoms and solid-state materials[59,60], and such beams can be created by utilizing polarization vortex beams[11]. Our quasicrystal lasing concept offers abundant possibilities for such studies and, more generally, for research on interactions between topological light and topological matter. It would be intriguing to pursue various types of photon and polariton condensation phenomena in optical structures created with our quasicrystal design principles: how would thermalization work and what kind of statistical distributions and coherence decay laws[61] could emerge in a system with no clear band edges or dispersion relations?

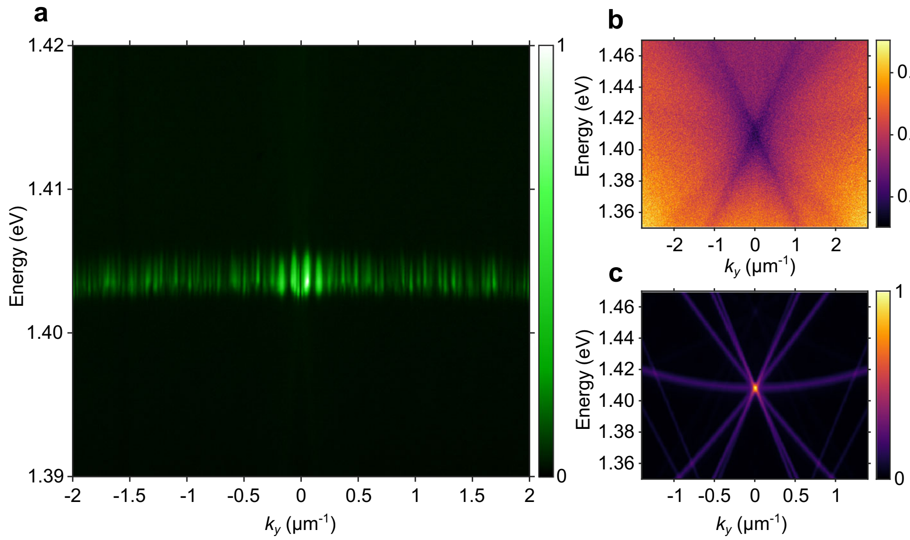

Fig. 4 | Angle-resolved features of plasmonic quasicrystal modes. a Wavevector-resolved spectrum of lasing action with topological charge -5, corresponding essentially to a crosscut of the angle-resolved image (Fig. 2a) at $k_x = 0$. The colorscale corresponds to normalized intensity. **b** Energy dispersion of the quasicrystal used to generate the lasing pattern shown in panel a measured as $1 - T$ where T is transmission. The dispersion is measured for bare nanoparticles with index-matching oil replacing the organic dye. Corresponding data for other samples are presented in Supplementary Fig. S15. **c** The calculated quasi-band structure is obtained by applying a structure-factor-based method[68] to the quasicrystal pattern, with the colorscale indicating the normalized weight of the band.

Finally, “inverting” our design method opens exciting possibilities: instead of lossy objects at the field minima, one can structure the gain medium to be located at the field maxima. This could be realized, for example, with semiconductor micropillars[62] or quantum dots. Apart from selecting the desired mode for lasing or condensation, this would bring in an interesting interplay with non-linear effects.

Methods

Sample fabrication

Electron beam lithography was used to fabricate quasicrystal arrays of cylindrical nanoparticles on borosilicate glass substrates ($n_r = 1.52$). The particles consisted of a 2 nm adhesion layer of titanium and a 50 nm layer of gold, and their nominal diameter was 240 nm (topological charges −3 and −5) or 260 nm (charge −4). The shape of the quasicrystal structures was circular with a diameter of 290 μm. For lasing experiments, the particles were immersed in a fluorescent dye solution (IR-140, 12 mM concentration). The dye was sealed between the substrate and another glass slide using press-to-seal silicone isolators (Merck) whose thickness was 0.8 mm. The solvent was a 2:1 mixture of benzyl alcohol and dimethyl sulfoxide in order to match the refractive index of the dye closely with the glass slides. For transmission experiments, the fluorescent dye was replaced with index-matching oil.

Experimental setup

Supplementary Fig. S16 shows a schematic of the optical setup that was used for both the transmission and lasing measurements. The samples were imaged using an objective (0.3 numerical aperture) whose back focal plane was magnified to a spectrometer entrance slit. The back focal plane (Fourier plane) contains the angular information of emission and corresponds to the reciprocal k-space. Therefore, each position on the slit represents a unique emission (or transmission) angle θ_y with respect to the sample normal. The spectrometer grating disperses the light to a charge-coupled device camera, whose pixel rows and columns are used to resolve the wavelength λ_0 and angle θ_y of the detected light, respectively. The $E(k)$ dispersions were then calculated using $E = hc/\lambda_0$ and $k_y = 2\pi/\lambda_0 \sin(\theta_y)$, where h is the Planck constant and c is the speed of light. The slit size in the measurements was set to 300 μm, which corresponds to a ± 0.37° angle around the sample normal or ±0.093 μm^{-1} crosscut around $k_x = 0$ in k-space at 1.41 eV. Note that the size of the features observed in the lasing patterns are smaller than the slit width. Therefore, we used the distance between the lasing spots in k-space to estimate the effective spectral resolution for the setup as 0.41 meV (see Supplementary Fig. S17 and Supplementary Note S3 for more details). Real space and angle-resolved (k-space) images of the sample emission were captured using two complementary metal-oxide semiconductor cameras placed at the image and Fourier planes of the optical setup. A real space iris was used to restrict the analyzed sample area to a single quasicrystal in each measurement.

In the transmission measurements, the sample was illuminated from the backside with diffused and focused white light from a commercial halogen lamp. The transmitted light was guided to the spectrometer slit without any filters in place. The transmission values were calculated as $T = I_t/I_r$, where I_t is the transmitted intensity and I_r is the reference intensity of the lamp measured through a substrate without nanoparticles.

In the lasing measurements, the quasicrystals were pumped optically with ultrafast laser pulses through the detection objective at room temperature. The pump laser had a center wavelength of 800 nm, a pulse length of 100 fs, bandwidth of 20 nm (full width at half maximum), and a repetition frequency of 1 kHz. A long pass filter (LP850) was used throughout the measurements to filter out pump reflections, and an additional band pass filter (FL880) was used while capturing the k-space images. The laser spot on the sample was a magnified image of a pump iris focused through a pump lens and the objective. A half- and a quarter-wave plate were used to make the pump pulses left-circularly polarized as they reach the sample. We have checked that the polarization handedness does not affect the results. A metal-coated neutral density wheel was used to control the pump fluence. The spatial intensity profile of the pump was nearly flat-top with the center of the spot being slightly more intense. All data shown here were integrated over multiple pulses: the shortest exposure time used in the cameras was 450 ms.

Pattern design

The ohmic losses in plasmonic lattices play a major role in the onset of lasing, with the least lossy usually being the one to lase[31]. Here we

https://doi.org/10.1038/s41467-024-53952-5

consider metallic nanoparticles as dampeners on the electric field similar to weights or clamps on a vibrating plate. The goal is to first identify the electric field pattern based on the symmetries in the system (group theory) and place the nanoparticles in a way that minimizes the losses in the selected mode. In its simplest form, the particles will not interact with the electric field if there is no field due to destructive interference at the particle position. The studied structures have the center of rotation at their center and are thus rotationally symmetric.

The design consists of three steps. First, a modified version of the density-wave method is used. While the method has previously been used to generate quasiperiodic structures[43,63], here we extend it to all irreducible representations (IRs) by considering phase-relations as derived from the rotational symmetry of the system. Previous studies using the density-wave method have not utilized the potential of the phase relations and thereby have been essentially limited to the IR whose eigenvalue is one, i.e., topological charge of one. The energy density minima of the IR with the highest topological charge are then selected as potential particle positions. Second, the scattering properties of the lattice are refined by reintroducing the quasiperiodicity in the form of a moiré-quasicrystal[64,65] obtained from n stacked gratings. We interpret the moiré patterns as effective unit cells and use them to discard the minima from the first step that are non-quasiperiodic. Third, the particle density is equalized to mitigate the formation of internal structures and to minimize additional effects coming from particle-particle interactions. These three steps are explained in detail below, and more information about them is available in Supplementary Note S2.

Empty-lattice electric fields

Let us first consider a two-dimensional system with n-fold rotational symmetry without any particles. In such a system we describe the electric field as a sum of n crossing plane waves with momenta $\mathbf{k}_j$:

$$\mathbf{E}_j(\mathbf{k}_j,\mathbf{r}) = e^{i\mathbf{k}_j\cdot\mathbf{r}}\begin{bmatrix} a_j \\ b_j \end{bmatrix} \text{ with } \mathbf{k}_j = |\mathbf{k}|\begin{bmatrix} \cos(j\cdot 2\pi/n) \\ \sin(j\cdot 2\pi/n), \end{bmatrix}$$

where a_j, b_j are the x- and y-components of each wave. They can be obtained for each IR from the eigenvalue equation

$$Sf = \epsilon f \text{ with} f = [a_1, b_1, a_2, b_2, \ldots]^T,$$

where S is the symmetry operator which rotates the system by $2\pi/n$. For a system of in-plane plane-waves, $S = R_s \otimes R$ where R_s is the shuffling matrix, which takes the wave $\mathbf{k}_j$ to $\mathbf{k}_{j+1}$, and R is the in-plane rotation matrix, which rotates the in-plane vector $[a_j,\ b_j]$. The eigenvalues ϵ describe the phase relation between adjacent waves and they are tabulated in character tables for different symmetry groups. Since ϵ originate from the rotational symmetry of the system, they are connected to the possible angular momentum states that can exist in the system[39], a connection that is explored more in Supplementary Note 1. Here we select the eigenvalue with $\epsilon = \epsilon_B = -1$ as it belongs to the same IR B as the lasing mode with the largest topological charge as seen from Eq. (1) in the main text. As a linearly polarized singlet state, the vector components of B contain equal amounts of opposite angular momenta making the total angular momentum of the beam zero. With the eigenvector f_B we can construct the electric field by summing the plane waves and find the energy density $\rho_B(\mathbf{r})$:

$$\rho_B(\mathbf{r}) = \left|\sum_j e^{i\mathbf{k}_j\cdot\mathbf{r}}\begin{bmatrix} a_{B,j} \\ b_{B,j} \end{bmatrix}\right|^2.$$

The energy density ρ can be similarly calculated for other IRs with other eigenvectors. It should be noted that ρ_A is produced by the standard density wave method when using f_A which corresponds to the eigenvalue $\epsilon = 1$, i.e., the phases of the waves are equal. From the low-intensity regions (nodes) of the interference pattern, one can identify locations where the interference is destructive and the energy density is low. As the nanoparticles have ohmic losses, they act as dampeners on the electric field. This interaction is minimized by placing particles in the nodes of the desired field. In practice, the particles are of finite size and there will be losses even if they are positioned directly at the field nodes. The losses for a set of particles are estimated from the amount of energy covered by the nanoparticle assembly, obtained as the integral of the energy density over the area of the structure:

$$E_{\text{loss}} \approx \int dA_{\text{particles}}\rho_{\text{IR}}(\mathbf{r}).$$

It is assumed that the configuration with the lowest losses (smallest E_{loss}) will start lasing. On a practical level, losses for the IR B case are minimized by placing particles in regions where $\rho_B(\mathbf{r}) \approx 0$. Due to the orthogonality of the IRs, they each have their own set of minima, which is of course crucial for our method. Values of E_{loss} for different IRs for the C_{12} sample are shown in Supplementary Fig. S18.

In the absence of particles, the energy of the mode is given by the empty lattice approximation $E = \|\mathbf{k}\|\hbar c/n_r$ which was set as $E \approx 1.41$ eV. The method can be generalized for other energies by changing the magnitude of $\mathbf{k}$. This does not change the structure of ρ_{IR}, but rather scales it by moving the minima closer to the origin or further apart.

Moiré quasicrystal

Our approach is different from previous plasmonic moiré patterns in which the quasi-lattice emerges from two lattices set at an angle[66]. We use moiré gratings to refine the quasiperiodicity in the points obtained in the first step described above by considering multiple gratings of width 2δ with π/n angles stacked on top of each other. This scheme yields a number of regions that are interpreted as the quasi-unit-cells (see Supplementary Fig. S19) allowing us to select only those minima which approximately satisfy the quasiperiodic condition in all n directions. In practice, the particle density is too low for plasmonic lasing when considering minima which fit in all of the gratings. The density can be increased by including regions that satisfy a partial moiré condition where only M gratings out of n are considered at once. The parameters M and δ are then tuned on a system-by-system basis so that roughly 10^5 minima remain. In the generation of C_{12}-samples a grating of period $p = 580$ nm with $\delta = 0.25p$ was used along with $M \geq 8$.

Density equalization

As a final optimization step, the particle density is equalized to make the bulk as uniform as possible. Having a larger minimal distance between particles reduces the particle-particle interactions which scale $\propto 1/r$ and eliminates regions of high particle density. Higher density regions might behave differently from the rest of the bulk causing the modes to localize in regions where they are not wanted. The density is reduced with an iterative method where the number of neighbors within a certain distance is calculated for all particles and those with the most neighbors are removed until the variance in the number of neighbors is reasonably small.

Distinction from periodic lasing structures

The emission patterns generated by our samples are the result of lasing in truly higher-order modes supported by the quasicrystal structure, distinguishing them from those generated by a trivial, periodic lasing mode that is simply modulated by the intricate nanoparticle pattern. This is supported by the slight differences in lasing wavelengths, linewidths, and thresholds observed in quasicrystals with different topological charges in lattices built to match the same wavelength, which implies that the underlying lasing mode is different in each case.

The quasicrystal samples contain all the possible modes enabled by the symmetry group in question, and the loss-driven design principles are used to enforce lasing in only one of them. If the observed emission patterns were the result of spatially modulated lasing of periodic origin, they would contain a combination of all the possible topological charges, which is not the case here.

Simulations

To numerically simulate the modes of the quasicrystal structure, we use the coupled-dipole approximation. The approximation is justified by the small size of the nanoparticles compared to the wavelength of the lasing action. The particles are approximated as in-plane dipole moments $\mathbf{p}_i = (p_i^x, p_i^y)$, which are coupled in a polarization-dependent way to all other dipoles, as in refs. [19,31]. The coupling strength between dipoles is defined according to the dipole orientation with respect to the vector $\mathbf{e}_L^j = (\mathbf{r}_i - \mathbf{r}_{i+j})/|\mathbf{r}_i - \mathbf{r}_{i+j}|$ connecting particles i and $i+j$, where $\mathbf{e}_T^j \cdot \mathbf{e}_L^j = 0$. For dipoles oriented longitudinally to $\mathbf{e}_L^j$, e.g., for horizontal polarization, the coupling is Ω_L, while for dipoles oriented transversely to $\mathbf{e}_L^j$, e.g., for vertical polarization, the coupling is Ω_T. Since the coupling between dipoles is highly directional and polarization-dependent, momentum and polarization are effectively coupled. The bare dipole oscillation frequency is $\omega_0 \gg \Omega_T \gg \Omega_L$. The modes are found from solving the equations

$$\ddot{\mathbf{p}}_i = \omega_0 \mathbf{p}_i + \sum_{j \neq i} \left[\frac{\Omega_L}{R_j^3} \left(\mathbf{p}_{i+j} \cdot \mathbf{e}_L^j \right) \mathbf{e}_L^j + \frac{\Omega_T}{R_j^3} \left(\mathbf{p}_{i+j} \cdot \mathbf{e}_T^j \right) \mathbf{e}_T^j \right],$$

where $R_j = |\mathbf{r}_i - \mathbf{r}_{i+j}|$. In the basis (p_i^x, p_i^y), the eigenmode gives the orientation of the electric dipole moment of each nanoparticle. Due to computational limitations, we simulate a smaller portion, 60 µm diameter, of the same larger structure that was used in the experiment. The eigenmodes are then classified into irreducible representations according to how they behave in terms of phase changes under rotational symmetry. The character ϵ_{IR} is calculated for each eigenmode $|P\rangle$ as $\epsilon_{\mathrm{IR}} = \langle P|S|P\rangle$, where S is the symmetry-operator which rotates the system by $2\pi/n$. In the far-field, each dipole behaves as a monochromatic point source, generating an Airy pattern. The electric field resulting from each nanoparticle in the far-field is expressed in terms of the dipole orientation as $\mathbf{E}_i(\mathbf{r}) \propto \mathbf{p}_i \mathcal{J}_1(\alpha|\mathbf{r} - \mathbf{R}_i|)/(\alpha|\mathbf{r} - \mathbf{R}_i|)$, where α is an inverse-length parameter that depends on the interparticle distance, and $\mathcal{J}_1$ is the first order regular Bessel function[67]. By summing all the individual nanoparticles' contributions $\mathbf{E}(\mathbf{r}) \propto \sum_i \mathbf{E}_i(\mathbf{r})$, we obtain the far-field pattern in real space. Information about the electric field polarization is obtained by performing a Fourier transformation of $\mathbf{E}(\mathbf{r})$ and constructing the Stokes parameters in the reciprocal space.

Data availability

The particle patterns generated in this work are provided as Supplementary Data 1–3 of this article. The raw lasing measurements for Figs. 2a, b and 3a, b are available at https://doi.org/10.6084/m9.figshare.27004522.v1.

Code availability

The code for generating the particle files is available at https://doi.org/10.5281/zenodo.13902435.

References

1. Teo, J. C. & Hughes, T. L. Topological defects in symmetry-protected topological phases. *Annu. Rev. Condens Matter Phys.* **8**, 211–237 (2017).
2. Rider, M. S. et al. A perspective on topological nanophotonics: current status and future challenges. *J. Appl. Phys.* **125**, 120901 (2019).
3. Ozawa, T. et al. Topological photonics. *Rev. Mod. Phys.* **91**, 015006 (2019).
4. Scheuer, J. & Orenstein, M. Optical vortices crystals: spontaneous generation in nonlinear semiconductor microcavities. *Science* **285**, 230–233 (1999).
5. Abo-Shaeer, J. R., Raman, C., Vogels, J. M. & Ketterle, W. Observation of vortex lattices in Bose-Einstein condensates. *Science* **292**, 476–479 (2001).
6. Zhen, B., Hsu, C. W., Lu, L., Stone, A. D. & Soljačić, M. Topological nature of optical bound states in the continuum. *Phys. Rev. Lett.* **113**, 257401 (2014).
7. Plotnik, Y. et al. Experimental observation of optical bound states in the continuum. *Phys. Rev. Lett.* **107**, 183901 (2011).
8. Hsu, C. W. et al. Observation of trapped light within the radiation continuum. *Nature* **499**, 188–191 (2013).
9. Doeleman, H. M., Monticone, F., den Hollander, W., Alù, A. & Koenderink, A. F. Experimental observation of a polarization vortex at an optical bound state in the continuum. *Nat. Photonics* **12**, 397–401 (2018).
10. Jin, J. et al. Topologically enabled ultrahigh-Q guided resonances robust to out-of-plane scattering. *Nature* **574**, 501–504 (2019).
11. Wang, B. et al. Generating optical vortex beams by momentum-space polarization vortices centred at bound states in the continuum. *Nat. Photonics* **14**, 623–628 (2020).
12. Bai, T. et al. Terahertz vortex beam generator based on bound states in the continuum. *Opt. Express* **29**, 25270–25279 (2021).
13. Kang, M. et al. Merging bound states in the continuum by harnessing higher-order topological charges. *Light Sci. Appl.* **11**, 228 (2022).
14. Wu, Y., Kang, L. & Werner, D. H. Active quasi-BIC optical vortex generators for ultrafast switching. *N. J. Phys.* **24**, 033002 (2022).
15. Zhang, T. et al. Twisted moiré photonic crystal enabled optical vortex generation through bound states in the continuum. *Nat. Commun.* **14**, 6014 (2023).
16. Sadrieva, Z. F. et al. Transition from optical bound states in the continuum to leaky resonances: role of substrate and roughness. *ACS Photonics* **4**, 723–727 (2017).
17. Azzam, S. I. et al. Single and multi-mode directional lasing from arrays of dielectric nanoresonators. *Laser Photonics Rev.* **15**, 2000411 (2021).
18. Ha, S. T. et al. Directional lasing in resonant semiconductor nanoantenna arrays. *Nat. Nanotechnol.* **13**, 1042–1047 (2018).
19. Heilmann, R., Salerno, G., Cuerda, J., Hakala, T. K. & Törmä, P. Quasi-BIC mode lasing in a quadrumer plasmonic lattice. *ACS Photonics* **9**, 224–232 (2022).
20. Miyai, E. et al. Lasers producing tailored beams. *Nature* **441**, 946–946 (2006).
21. Iwahashi, S. et al. Higher-order vector beams produced by photonic-crystal lasers. *Opt. Express* **19**, 11963–11968 (2011).
22. Kodigala, A. et al. Lasing action from photonic bound states in continuum. *Nature* **541**, 196–199 (2017).
23. Huang, C. et al. Ultrafast control of vortex microlasers. *Science* **367**, 1018–1021 (2020).
24. Guan, J. et al. Quantum dot-plasmon lasing with controlled polarization patterns. *ACS Nano* **14**, 3426–3433 (2020).
25. Guan, J. et al. Engineering directionality in quantum dot shell lasing using plasmonic lattices. *Nano Lett.* **20**, 1468–1474 (2020).
26. Wang, Z., Liang, Y., Beck, M., Scalari, G. & Faist, J. Topological charge of finite-size photonic crystal modes. *Phys. Rev. B* **102**, 045122 (2020).
27. Hwang, M.-S. et al. Ultralow-threshold laser using super-bound states in the continuum. *Nat. Commun.* **12**, 1–9 (2021).
28. Wu, M. et al. Bound state in the continuum in nanoantenna-coupled slab waveguide enables low-threshold quantum-dot lasing. *Nano Lett.* **21**, 9754–9760 (2021).

29. Asamoah, B. O. et al. Finite size mediated radiative coupling of lasing plasmonic bound state in continuum. *arXiv:2206.05011* (2022).
30. Mohamed, S. et al. Controlling topology and polarization state of lasing photonic bound states in continuum. *Laser Photonics Rev.* **16**, 2100574 (2022).
31. Salerno, G. et al. Loss-driven topological transitions in lasing. *Phys. Rev. Lett.* **129**, 173901 (2022).
32. Sang, Y.-G. et al. Topological polarization singular lasing with highly efficient radiation channel. *Nat. Commun.* **13**, 6485 (2022).
33. Ren, Y. et al. Low-threshold nanolasers based on miniaturized bound states in the continuum. *Sci. Adv.* **8**, eade8817 (2022).
34. Zhai, Z. et al. Multimode vortex lasing from dye-TiO_2 lattices via bound states in the continuum. *ACS Photonics* **10**, 437–446 (2023).
35. Berghuis, A. M. et al. Room temperature exciton-polariton condensation in silicon metasurfaces emerging from bound states in the continuum. *Nano Lett.* **23**, 5603–5609 (2023).
36. Qiao, Z. et al. High orbital angular momentum lasing with tunable degree of chirality in a symmetry-broken microcavity. *Optica* **10**, 846–853 (2023).
37. Li, R. et al. Generating large topological charge laguerre–gaussian beam based on 4k phase-only spatial light modulator. *Chin. Opt. Lett.* **20**, 120501 (2022).
38. Miao, P. et al. Orbital angular momentum microlaser. *Science* **353**, 464–467 (2016).
39. Carlon Zambon, N. et al. Optically controlling the emission chirality of microlasers. *Nat. Photonics* **13**, 283–288 (2019).
40. Kaliteevski, M. A. et al. Two-dimensional Penrose-tiled photonic quasicrystals: from diffraction pattern to band structure. *Nanotechnology* **11**, 274 (2000).
41. Notomi, M., Suzuki, H., Tamamura, T. & Edagawa, K. Lasing action due to the two-dimensional quasiperiodicity of photonic quasicrystals with a Penrose lattice. *Phys. Rev. Lett.* **92**, 123906 (2004).
42. Vitiello, M. S. et al. Photonic quasi-crystal terahertz lasers. *Nat. Commun.* **5**, 5884 (2014).
43. Che, Z. et al. Polarization singularities of photonic quasicrystals in momentum space. *Phys. Rev. Lett.* **127**, 043901 (2021).
44. Wang, W. et al. The rich photonic world of plasmonic nanoparticle arrays. *Mater. Today* **21**, 303–314 (2018).
45. Kravets, V. G., Kabashin, A. V., Barnes, W. L. & Grigorenko, A. N. Plasmonic surface lattice resonances: a review of properties and applications. *Chem. Rev.* **118**, 5912–5951 (2018).
46. Zhou, W. et al. Lasing action in strongly coupled plasmonic nanocavity arrays. *Nat. Nanotechnol.* **8**, 506–511 (2013).
47. Hakala, T. K. et al. Lasing in dark and bright modes of a finite-sized plasmonic lattice. *Nat. Commun.* **8**, 13687 (2017).
48. Wang, D., Wang, W., Knudson, M. P., Schatz, G. C. & Odom, T. W. Structural engineering in plasmon nanolasers. *Chem. Rev.* **118**, 2865–2881 (2018).
49. Dresselhaus, M. S., Dresselhaus, G. & Jorio, A. *Group Theory: Application to the Physics of Condensed Matter* (Springer Science & Business Media, 2007).
50. Cuerda, J., Taskinen, J. M., Källman, N., Grabitz, L. & Törmä, P. Observation of Quantum metric and non-Hermitian Berry curvature in a plasmonic lattice. *Phys. Rev. Res.* **6**, L022020 (2024).
51. Daskalakis, K. S., Väkeväinen, A. I., Martikainen, J.-P., Hakala, T. K. & Törmä, P. Ultrafast pulse generation in an organic nanoparticle-array laser. *Nano Lett.* **18**, 2658–2665 (2018).
52. Rosales-Guzmán, C., Ndagano, B. & Forbes, A. A review of complex vector light fields and their applications. *J. Opt.* **20**, 123001 (2018).
53. Zhao, Y. & Wang, J. High-base vector beam encoding/decoding for visible-light communications. *Opt. Lett.* **40**, 4843–4846 (2015).
54. Willner, A. E., Pang, K., Song, H., Zou, K. & Zhou, H. Orbital angular momentum of light for communications. *Appl. Phys. Rev.* **8**, 041312 (2021).
55. Liu, J. et al. Direct fiber vector eigenmode multiplexing transmission seeded by integrated optical vortex emitters. *Light Sci. Appl.* **7**, 17148 (2018).
56. Shen, Y. et al. Optical vortices 30 years on: OAM manipulation from topological charge to multiple singularities. *Light Sci. Appl.* **8**, 90 (2019).
57. Wiersma, D. S. The physics and applications of random lasers. *Nat. Phys.* **4**, 359–367 (2008).
58. Padiyakkuth, N., Thomas, S., Antoine, R. & Kalarikkal, N. Recent progress and prospects of random lasers using advanced materials. *Mater. Adv.* **3**, 6687–6706 (2022).
59. Takahashi, H. T., Proskurin, I. & Kishine, J.-i Landau level spectroscopy by optical vortex beam. *J. Phys. Soc. Jpn* **87**, 113703 (2018).
60. Cao, B., Grass, T., Solomon, G. & Hafezi, M. Optical flux pump in the quantum Hall regime. *Phys. Rev. B* **103**, L241301 (2021).
61. Sieberer, L. M., Huber, S. D., Altman, E. & Diehl, S. Dynamical critical phenomena in driven-dissipative systems. *Phys. Rev. Lett.* **110**, 195301 (2013).
62. Amo, A. & Bloch, J. Exciton-polaritons in lattices: a non-linear photonic simulator. *Comptes Rendus Phys.* **17**, 934–945 (2016).
63. Rechtsman, M. C., Jeong, H.-C., Chaikin, P. M., Torquato, S. & Steinhardt, P. J. Optimized structures for photonic quasicrystals. *Phys. Rev. Lett.* **101**, 073902 (2008).
64. Lubin, S. M., Zhou, W., Hryn, A. J., Huntington, M. D. & Odom, T. W. High-rotational symmetry lattices fabricated by moiré nanolithography. *Nano Lett.* **12**, 4948–4952 (2012).
65. Mahmood, R., Ramirez, A. V. & Hillier, A. C. Creating two-dimensional quasicrystal, supercell, and moiré lattices with laser interference lithography: Implications for photonic bandgap materials. *ACS Appl. Nano Mater.* **4**, 8851–8862 (2021).
66. Zhang, Y. et al. Unfolded band structures of photonic quasicrystals and moiré superlattices. *Phys. Rev. B* **105**, 165304 (2022).
67. Guo, R., Nečada, M., Hakala, T. K., Väkeväinen, A. I. & Törmä, P. Lasing at *K* points of a honeycomb plasmonic lattice. *Phys. Rev. Lett.* **122**, 013901 (2019).
68. Heilmann, R., Arjas, K., Hakala, T. K. & Törmä, P. Multimode lasing in supercell plasmonic nanoparticle arrays. *ACS Photonics* **10**, 3955–3962 (2023).

Acknowledgements
This work was supported by the Academy of Finland under Project No. 349313. K.A. acknowledges financial support by the Vilho, Yrjö and Kalle Väisälä Foundation. J.M.T. acknowledges financial support by the Magnus Ehrnrooth Foundation. G.S. has received funding from the European Union's Horizon 2020 research and innovation program under the Marie Skłodowska-Curie grant agreement No 101025211 (TEBLA), and from the Academy of Finland under Project No. 13354165. The work is part of the Research Council of Finland Flagship Program, Photonics Research and Innovation (PREIN), decision number 346529, Aalto University. Part of the research was performed at the OtaNano Nanofab cleanroom (Micronova Nanofabrication Center), supported by Aalto University. We thank Evgeny Mamonov for advice with the experimental setup.

Author contributions
P.T. initiated and supervised the project. K.A. developed the quasicrystal design method and G.S. did the coupled dipole calculations. J.M.T. fabricated the samples and performed all the experiments except the coherence measurements. R.H. performed the coherence measurements. All authors discussed the results and wrote the manuscript together.

Competing interests
The authors declare no competing interests.

Additional information

Supplementary information The online version contains supplementary material available at https://doi.org/10.1038/s41467-024-53952-5.

Correspondence and requests for materials should be addressed to Päivi Törmä.

Peer review information *Nature Communications* thanks Philippe St-Jean, and the other, anonymous, reviewer(s) for their contribution to the peer review of this work. A peer review file is available.